Check for updates

Optics EXPRESS

Patterned achromatic elliptical polarizer for short-wave infrared imaging polarimetry

LINAN JIANG,[1,*] SAWYER MILLER,[1] XINGZHOU TU,[1] MATT SMITH,[2] YANG ZOU,[2] FRANCIS REININGER,[3] AND STANLEY PAU[1]

[1] *James C. Wyant College of Optical Sciences, University of Arizona, Tucson, AZ 85721, USA*
[2] *Axometrics, Inc., Huntsville, AL 35806, USA*
[3] *Spectral Imaging Laboratory, Pasadena, CA 91107, USA*
[*] *jiangl@arizona.edu*

Abstract: Short-wave infrared (SWIR) imaging polarimetry has widespread applications in telecommunication, medical imaging, surveillance, remote-sensing, and industrial metrology. In this work, we design, fabricate, and test an achromatic SWIR elliptical polarizer, which is a key component of SWIR imaging polarimetry. The elliptical polarizer is made of a patterned linear polarizer and a patterned optical elliptical retarder. The linear polarizer is a wire grid polarizer. The elliptical retarder is constructed with three layers of nematic phase A-plate liquid crystal polymer (LCP) films with different fast axis orientations and physical film thicknesses. For each LCP layer, four arrays of hexagonal patterns with individual fast-axis orientations are realized utilizing selective linearly polarized ultraviolet (UV) irradiation on a photo-alignment polymer film. The Mueller matrices of the optical filters were measured in the wavelength range 1000 nm to 1600 nm and compared with theory. Our results demonstrate the functionality and quality of the patterned retarders with normalized analyzer vector parameter deviation below 7% over this wavelength range. To the best of our knowledge, this work represents the first polymer-based patterned elliptical polarizer for SWIR polarimetry imaging applications.

© 2022 Optica Publishing Group under the terms of the Optica Open Access Publishing Agreement

1. Introduction

The achromatic polarizer is an important optical component in polarimetry, where it is used to select optical signals of a specific polarization state over a wavelength band. Recent developments in achromatic polarizers, such as linear, circular, or elliptical polarizers, are mostly for applications in the visible wavelength range of 450 nm to 650 nm, where the polarization of light in the entire visible spectrum can be measured [1–10]. Polarization imaging in the short-wave infrared (SWIR) has recently attracted a growing interest in research and development because of the unique wavelength range of 900 nm to 2500 nm. The longer wavelengths can penetrate deeper into obscuring layers, such as haze, fog, smoke and biological tissues. They can also be absorbed by the mechanism of molecular vibrations in unique wavelength bands for remote identification of chemicals [11]. In addition, water vapor, fog, and materials such as silicon are transparent in SWIR. The 1100 nm to 1350 nm transmission window, located between water peaks at ~970 nm and ~1444 nm, has been used for in vivo bioimaging [12,13]. An observed object often emits light in the mid-wave infrared and long-wave infrared range, while reflecting or absorbing SWIR light [11]. Objects with color and similar appearances in the visible spectrum can be distinguished in SWIR with high-contrast images. Furthermore, SWIR is invisible to the human eye. Therefore, SWIR imaging polarimetry has potential for many applications in telecommunication [14], surveillance [15,16], remote sensing [17–19], medical imaging [12,20] and industrial metrology [21,22]. The development of high-performance indium gallium arsenide (InGaAs) [23,24] and CQD CMOS sensors [25,26] with extended spectral range makes SWIR imaging now possible and practical. In contrast, commonly used silicon sensors only work for applications with a wavelength up to about 1000 nm. Previously, linear Stokes polarimetry in the SWIR was enabled

#445253 https://doi.org/10.1364/OE.445253
Journal © 2022 Received 7 Oct 2021; revised 7 Dec 2021; accepted 17 Dec 2021; published 4 Jan 2022

Optics EXPRESS

through a polarizer of a wire grating construction, fabricated by patterning aluminum thin film on a transparent substrate [27]. To the best of our knowledge, optical filters, which can be used for measurement of full Stokes parameters of broadband SWIR light, 1000 nm to 1600 nm, currently do not exist.

In this paper, we report on the design of an achromatic elliptical polarizer consisting of a multi-layer retarder and a linear elliptical polarizer for SWIR imaging. This design of the achromatic elliptical polarizer has two components: a retarder and a polarizer. We also present, for the first time, the fabrication and testing of the multi-layer retarder for the SWIR wavelength range. The achromatic elliptical polarizers are designed for a SWIR multi-modal artificial compound eye (ACE) camera [28] where the elliptical polarizers and dichroic bandpass filters are placed on either side of the aperture stop plane.

2. Design

At a constant temperature, the birefringence dispersion, Δn, of a liquid crystal film at non-resonant optical frequency regions can be described by a single band dispersion as a function of wavelength of the incident light λ [29]:

$$\Delta n(\lambda) = G\frac{\lambda^2\lambda^{*2}}{\lambda^2 - \lambda^{*2}} \tag{1}$$

Here λ^*, the mean resonance wavelength of the band, is a material property of birefringent film. G is the proportionality constant, approximately linearly proportional to the film physical thickness, d. For convenience, we relate the linear retardance of an LCP film, $\Delta\phi$, to the film physical and retardance thickness, d and t, respectively:

$$\Delta\phi(\lambda,\ d) = \frac{2\pi}{\lambda}\Delta n(\lambda)d = C\frac{\lambda\lambda^{*2}}{\lambda^2 - \lambda^{*2}}t \tag{2}$$

In Eq. (2), d and C, independent of wavelength, are physical thickness and a material property relating to the LCP film, respectively. The retardance thickness, t, a normalized parameter unique to a given LCP film, is defined by averaging two retardance values at 450 nm and 650 nm. Linear retardance thickness $t = 1$ is defined for the average linear retardance of 180 degrees as described in Eq. (3) [9]:

$$t = \frac{1}{180}\left[\frac{\Delta\phi(450nm,\ \ d) + \Delta\phi(\ 650nm,\ \ d)}{2}\right] \tag{3}$$

Samples of single-layer A-plate LCP film (RMM141C from EMD Chemicals) on a glass substrate with various physical thicknesses were made to evaluate the relationship between linear retardance and wavelength. Polarization parameters of the LCP films were measured using an Axometrics AxoScan Mueller Matrix Polarimeter for the wavelength 400 nm to 800 nm and a custom-configured polarimeter for 1000 nm to 1600 nm. The measurement results and the theoretical curves based on Eq. (2) are summarized in Fig. 1(a). The theoretical curves show good fits with the measured data, in the wavelengths range from 400 nm to 1600 nm, for all three samples with different LCP physical thicknesses.

A patterned micro-retarder device, 22 mm × 19 mm in size, is designed to consist of arrays of a four-retarder unit, R1, R2, R3 and R4, as shown in Fig. 1(b). Each retarder has a pattern of a hexagon with a side of 520 µm, and the four retarders are spatially arranged in their relative positions. In our previous work, we had shown that an achromatic elliptical polarizer could be obtained utilizing a combination of multi-layer retarders and one linear polarizer for applications in the visible wavelength range 450 nm to 650 nm [9]. The method defines a merit function considering the dispersion of the material, Eq. (2), and minimizes the analyzer vector variation in the 450 nm to 650 nm wavelength range. The optimized design parameters to achieve achromatic performance of the analyzer vector, *i.e.* the fast-axis angles, thicknesses of the linear retarders and

Optics EXPRESS

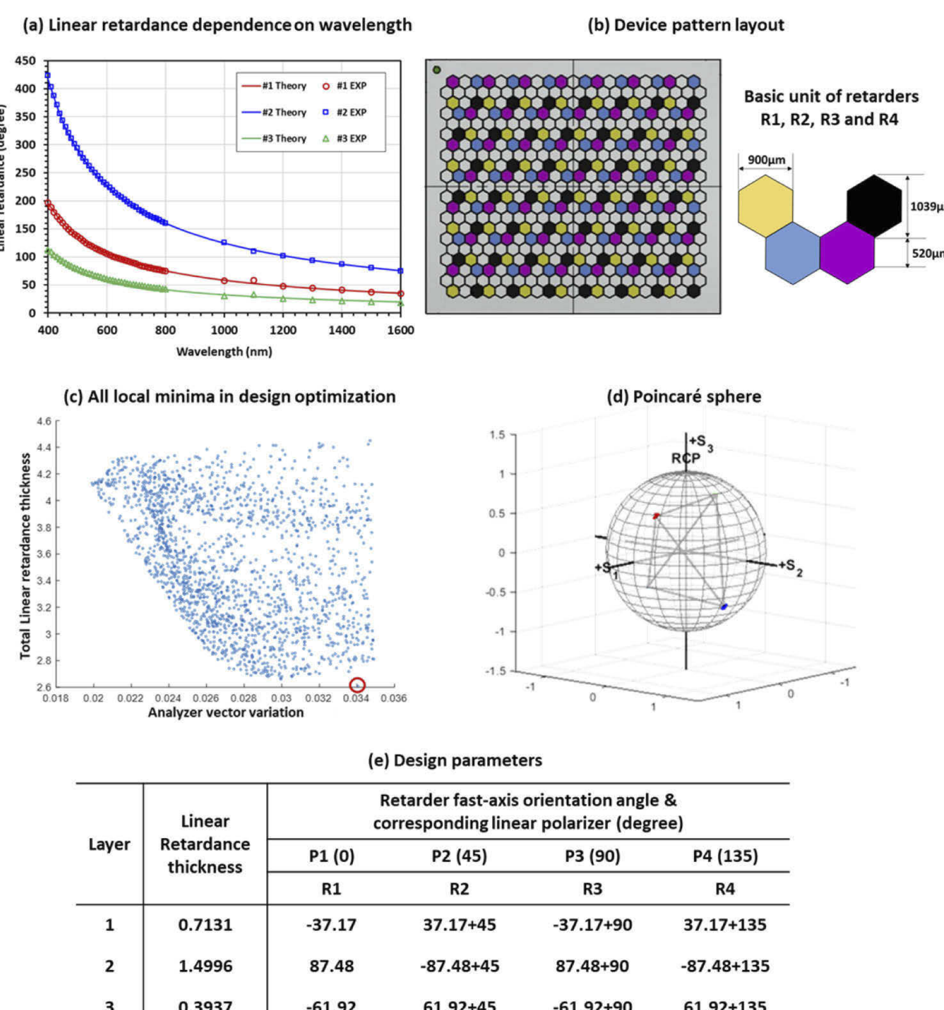

Layer	Linear Retardance thickness	Retarder fast-axis orientation angle & corresponding linear polarizer (degree)			
		P1 (0)	P2 (45)	P3 (90)	P4 (135)
		R1	R2	R3	R4
1	0.7131	-37.17	37.17+45	-37.17+90	37.17+135
2	1.4996	87.48	-87.48+45	87.48+90	-87.48+135
3	0.3937	-61.92	61.92+45	-61.92+90	61.92+135

Fig. 1. (a) A summary of measurement and theoretical results of LCP film linear retardance in the wavelength range of 400 nm to 1600 nm for three single-layer LCP samples is shown. (b) Illustration shows a micropatterned elliptical retarder device constructed by arrays of unit retarders R1, R2, R3 and R4. (c) Each point represents one possible design of an achromatic elliptical polarizer with local minima in the total film retardance thickness. The final design (circled in red) has a small total retardance thickness of 2.6, an analyzer vector variation of 3.41% and an EWV value of 11.56. (d) The analyzer vectors of the four achromatic elliptical polarizer output states are shown on the Poincaré sphere, forming a tetrahedron [30]. (e) Table lists the design parameters, including the thicknesses of the three LCP layers, fast-axis orientation angles for the four retarders, R1, R2, R3 and R4, in each layer, and the corresponding angles for the four linear polarizers, P1, P2, P3 and P4.

the transmission axis angle of the linear polarizer, are obtained using a multivariable constrained nonlinear solver. For the present design in the SWIR wavelength range, the same method can be applied as the results in Fig. 1(a) confirm that the LCP dispersion follows a single-band dispersion model of Eq. (2). However, new challenges arise for the SWIR applications. As shown in Fig. 1(a), the LCP film retardance is approximately inversely proportional to the wavelength, decreasing with increasing wavelength and nearly approaching a constant towards the SWIR

wavelength range, particularly for thinner films. Consequently, much thicker LCP films and larger numbers of LCP layers are necessary to realize an achromatic SWIR elliptical polarizer. When the same optimization approach for the 450 nm to 650 nm wavelength was used for the SWIR design, i.e. solving for a global minimum, the equally weighed variance (EWV) could be minimized to a theoretical value of 10 [30], while analyzer vector variation could be kept to a value of 2.22%. However, the film thicknesses for this optimization are too large to be physically realizable and repeatable under existing processing conditions. Therefore, a unique constraint on LCP film retardance thickness, i.e. each LCP layer retardance thickness is set to be less than 1.5, is enforced to warrant physically realizable film thicknesses in the SWIR design optimization. Possible designs with local minima of the total film retardance thickness were explored as presented in Fig. 1(c). Consequently, the design with the smallest total retardance thickness of 2.6 while keeping each layer retardance thickness below 1.5 was chosen (circled in red); this design corresponds to an analyzer vector variation of 3.41% and an EWV value of 11.56. The designed achromatic elliptical polarizer output states on the Poincaré sphere are shown in Fig. 1(d), forming a tetrahedron [30]. The design parameters, including the number of layers, retarder physical thickness, and local fast-axis orientation angle in each layer for the four retarders, R1, R2, R3 and R4, are summarized in a table in Fig. 1(e). This micro-retarder is designed to work with a linear polarizer device, having identical dimensions and corresponding polarization angles, fabricated on a separate substrate. Specifically, the four retarder arrays, R1, R2, R3 and R4, are aligned to operate with the four polarizer arrays, P1, P2, P3 and P4, with polarization angles of 0, 45, 90 and 135 degrees, respectively, as shown in Fig. 1(e). In this work, we focus on the design and fabrication of the retarder device. The patterned linear polarizer device is a custom aluminum wire grid nanowire polarizer made by Moxtek (Moxtek Inc., Orem UT, USA). The fabrication process of the linear polarizer is described elsewhere [31].

There are four on-chip test squares, each 11mm×11 mm in size representing the four retarders, R1, R2, R3 and R4, respectively, on each wafer to facilitate in-process inspections of the retardance and fast-axis orientation of the patterned retarders during the fabrication process. These test squares are necessary for measurements using the polarimeter with a source light beam size of about 5 mm in diameter, since the 520µm-side hexagonal patterns are too small for such measurements.

3. Materials and experimental methods

Double-side polished Corning Gorilla glass wafers (Valley Design Corp., Santa Cruz CA) were used as the substrate for the fabrication of the multi-layer retarder. The wafers are 0.55 mm thick and 100 mm in diameter with excellent optical transmittance over the entire wavelength range of 400 nm to 2000nm. They were cleaned using semiconductor grade acetone and isopropyl alcohol (IPA), and blow-dried with nitrogen prior to the fabrication process.

Linearly photo-polymerizable polymer ROP108 (LPP) (Rolic Technologies) was used as the photo-alignment material. Local orientation in the LPP can be obtained by selective exposure of linearly polarized ultraviolet radiation (LPUV). Consequently, local fast–axis orientations of the LCP film that is spin-coated directly on top of the LPUV-patterned LPP film are defined. In this work, selective LPUV was achieved using UV exposure of a MA6 aligner through a linear polarizer (Bolder Vision Optik, Inc.) and a photomask.

LCP RMM141C (EMD Chemicals) was used in this work to fabricate the micro-retarders. LCP solutions with various concentrations were obtained to achieve various physical film thicknesses. In addition, photoresist Shipley Microposit s1813 and developer MF-319 (MicroChem, Corp. MA) were used to fabricate the metal alignment marks for lithography patterning of the multiple retarder layers.

Quantitative measurements on the LCP films and retarders, including film thickness and transmissions, were performed using a Veeco-Dektak 150 surface-profilometer and a Cary 5000

spectrometer, respectively. Polarization characteristics, *i.e.* Mueller matrices, were obtained using an Axometrics AxoScan polarimeter for 400nm to 800nm wavelength range and a custom-configured Axometrics AxoScan with InGaAs detectors and bandpass filters (Thorlabs) for 1000 nm to 1600 nm wavelength range. For each polarization measurement, the stage of the Mueller matrix polarimeter is leveled and calibrated to set zero-degree polarization angle of the stage in reference to the angle of a fixed flat edge on the stage. Each sample wafer has a primary flat and a secondary flat with a 90-degree angle between them. We define the fast axis angle of zero on the sample when its primary flat is aligned with the reference edge on the stage. During the Mueller matrix measurements, the sample is fixed on the stage, with the polymer film-side facing up while the glass substrate in contact with the stage surface, where the measurement location on the sample is positioned right at the center of the light beam, which passes through the sample substrate with a zero-degree angle of incidence. The polarization measurements obtained the full Mueller matrices through a wavelength range of 400 nm to 1600 nm. The Mueller matrix as a function of wavelength can be further analyzed using the Lu-Chipman decomposition to determine important characteristics of the sample including diattenuation, retardance, and depolarization [14]. From this matrix decomposition and analysis, it can be determined whether or not the design parameters are achieved in the fabricated devices. Furthermore, the data on each layer collected through the fabrication process are used to analyze errors in the fabrication, which provide important information for optimizing the fabrication process.

A laser dicing saw (DISCO Hi-Tec America, Inc. CA, USA) was used to dice the wafer into individual micro-retarder filter devices, and to obtain the four test squares from the glass substrate.

4. Micro-retarder fabrication

Each 100mm-diameter glass wafer has six micro-retarder devices. First, metal alignment marks and device orientation marks were fabricated on each wafer using the lift-off technique. A 1.3μm-thick photoresist (Shipley Microposit s1813) was spin-coated onto an O_2-plasma-treated clean glass wafer. After baking at 115°C for 60 seconds on a hot plate, the photoresist layer was exposed using a MA6 aligner through a photomask with UV light. After the development of the patterned photoresist in developer MF-319, a 100nm-thick aluminum layer was deposited on the photoresist layer using a Temescal electron beam evaporator. The wafer was then immersed in a bath of acetone at room temperature, where the photoresist and the aluminum layer on top of the photoresist were removed from the substrate, obtaining the aluminum alignment/orientation marks on the substrate.

Next, the retarder device was fabricated in three steps corresponding to the three retarder layers. A similar fabrication process was used to obtain each retarder layer. In brief, for the first retarder layer, LPP was spin-coated on the glass wafer at a speed of 2500 rpm to obtain a uniform thin layer. The wafer was baked on a hot plate at 170°C for 10 minutes, and cooled down to room temperature. A set of four photomasks was subsequently used to define the four retarder pattern arrays where the local fast-axis orientations in the patterns were defined in LPP by UV exposures through a linear polarizer, i.e. LPUV, at four different angles. An additional photomask was used to set the background (negative field) fast-axis orientation at a random angle using LPUV. The five processes of LPUV patterning, each at about 2000mJ/cm^2, used the same set of alignment marks. Upon the completion of LPP patterning, an LCP solution was spin-coated immediately on the LPUV patterned LPP at room temperature to obtain the desired physical thickness. The wafer was baked at 52°C for one minute to evaporate the solvent, and the LCP film was cured using a flood UV exposure at an appropriate dosage according to the LCP film physical thickness. A 100nm-thick SiO_2 was evaporated using the Temescal evaporator on top of the cured LCP, which served as a barrier layer between the retarder layers. Similarly, using the same alignment marks, the second and the third patterned retarder layers were fabricated subsequently on top of

the first patterned retarder layer. The fabrication process was completed after deposition of a 100nm-thick SiO_2 as a protection layer.

Figure 2(a) is a schematic showing the cross-sectional view of the three retarder layers fabricated on the glass substrate. Patterns in each layer have four different fast-axis angles based on the design, and corresponding patterns in the three retarder layers are aligned. Figure 2(b) illustrates 3D views of a micro-retarder device through the fabrication process. In each retarder layer, four non-overlapping retarder arrays, R1, R2, R3 and R4, were obtained by four individual exposures through four different photomasks at four different linear polarization fast-axis angles. In addition, the corresponding patterns in the three retarder layers have the same physical locations; however, their retardance and fast-axis orientation are different in the three retarder layers as tabulated in Fig. 1(e).

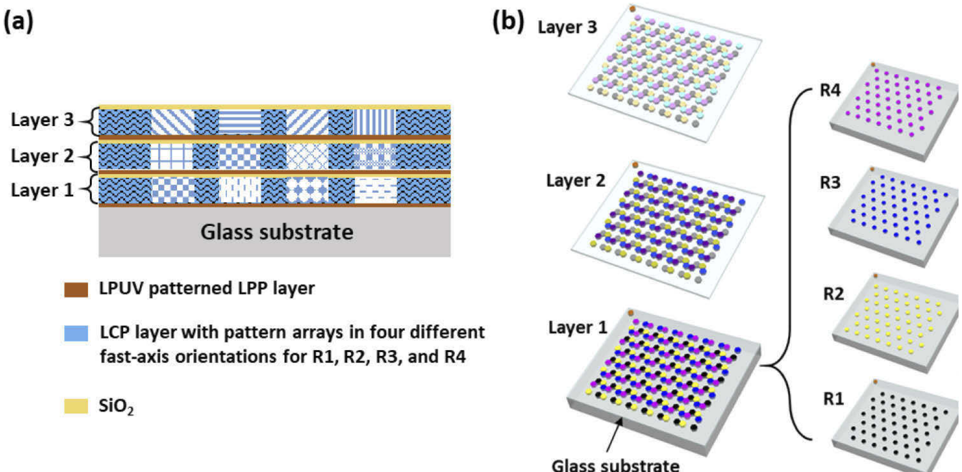

Fig. 2. Retarder fabrication: (a) A cross-sectional view shows the three retarder layers, each consisting of four retarders. The pattern positions are aligned in all three retarder layers, but their fast-axis orientations are different from layer to layer. (b) 3D views of each layer are shown exhibiting spatial relationship among the four retarder pattern arrays, R1, R2, R3, and R4, in each retarder layer. The patterned arrays are aligned by using alignment marks; each array in each layer has the same retardance (i.e. physical thickness) but a different fast-axis orientation.

The design retardance thicknesses for retarder Layer 1 and Layer 3 with reference to Eq. (3) are 0.7131 and 0.3937, respectively, which can be obtained by spin-coating of single LCP films at concentrations of about 15% to 30% (w/w) LCP in Toluene. However, the retardance thickness for retarder Layer 2 is 1.4996, which requires more than 40% (w/w) LCP in Toluene. The high concentration of LCP solution resulted in poor uniformity in the coating thickness of the film. Moreover, the interaction between the LCP molecules with LPUV patterned species on the LPP surface is short-ranged [32]. Therefore, LCP molecules are not aligned beyond a certain distance from the aligning surface of the LPP. Simply increasing the LCP physical film thickness by using a high concentration LCP solution cannot achieve the design retardance thickness of 1.4996. It is reported that the morphology of a surface can contribute physically to the anisotropic interaction between an LCP and the surface [32,33]. For retarder Layer 2, a two-step process was used to obtain the design retardance thickness. First, an LCP solution about 30% (w/w) in Toluene was spin-coated on top of the LPUV patterned LPP alignment layer. The aligned LCP film was cured using UV to obtain an aligned LCP film. A second coating of the same solution was spin-coated directly on top of the cured LCP. After baking at 52°C, the second LCP was aligned based on the

Optics EXPRESS

morphology of the first LCP film. After curing the second LCP film using UV light, the retarder Layer 2 was realized with the design retardance thickness.

A photo of a fabricated retarder device is shown in Fig. 3(a), where the device is illuminated from the back using LED bulbs and viewed through crossed linear polarizers. The photo displays the array pattern of the hexagons with uniform colors and shades. A microscope image of four of the elliptical retarder hexagons is shown in Fig. 3(b), revealing sharp edges. The hexagons are in the correct spatial positions, as prescribed by the design of Fig. 1(b), demonstrating good alignment between the three retarder layers. Different appearances in colors for the four patterns are seen through a linear polarizer, which reflect the differences in design in their eigenpolarizations. Figure 3(c) shows a close-up view of the pattern, without a linear polarizer, to reveal the morphology of the aligned LCP in each hexagon. The LCP alignment orientations in the four retarders and in the background (negative field), indicated by the red arrows, demonstrate the uniformity of the LPUV patterning of the LPP, as well as the effectiveness of the LCP alignment on the LPP. The morphology of the cured LCP also confirms its ability to serve as an aligning surface for a second LCP film directly on top of the cured LCP film. Pictures of the wire grid polarizer, viewed with no polarization analyzer in Fig. 3(d) and through a linear polarization analyzer in Fig. 3(e), show the same pattern arrays with corresponding polarizer transmission axis orientations.

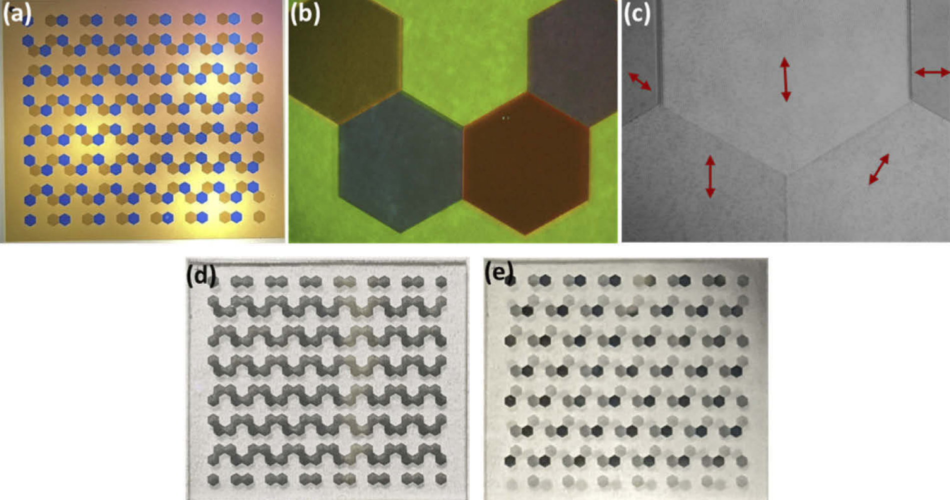

Fig. 3. (a) A photo of a fabricated micro-retarder array device viewed through crossed linear polarizers is shown. The device is back-illuminated by LED bulbs. (b) A polarized microscope image shows a unit of four hexagonal retarders. The colors shown in the four hexagonal patterns and in the background are attributed to material dispersion when imaging through a linear polarizer. (c) A close-up microscope image, without linear polarizer, reveals local LCP alignment orientations in the four retarders and in the background, marked by the red arrows. (d) and (e) Photos of wire grid linear polarizers are shown under direct light and through a wire grid linear polarizer, respectively.

The four on-chip test squares, corresponding to the four elliptical retarders, were characterized using a custom-configured Axometrics AxoScan polarimeter with InGaAs detectors for the 1000 nm to 1600 nm wavelength range. Mueller matrices of the four test squares were measured, and the linear retardance, circular retardance, and retardance orientation over the SWIR wavelength range are summarized in Fig. 4(a)-(d). The linear and total retardance for the four test squares are identical, demonstrating excellent uniformity of film thickness and patterning across the

entire wafer. Measurement of the circular retardance shows nearly identical magnitude for each square, with only the sign of circular retardance, i.e. handedness, differing. The retardance orientations also confirm the uniformity across the wafer. The results show the correct local fast-axis orientations for the four retarders according to the design, and the control of the fast-axis orientation angles in the LPUV processes is reliable.

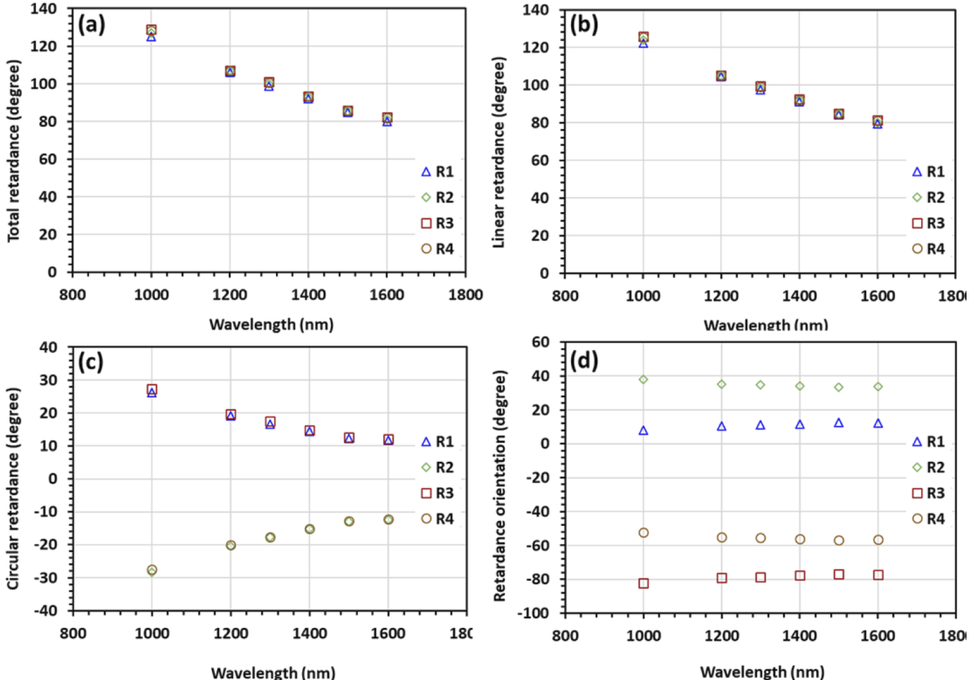

Fig. 4. Mueller matrix measurement data from the four on-chip test squares are plotted as a function of wavelength. The plots are (a) linear retardance, (b) total retardance, (c) circular retardance and (d) retardance orientation. Data at 1100 nm wavelength are not included in the figures due to poor calibration output at this particular wavelength.

Two important performance metrics of the elliptical polarizer are the flatness of the wavelength response and the width of the operating wavelength range. The analyzer vector for the four elliptical polarizers are plotted on the Poincaré sphere in Fig. 5(a) for 1000 nm to 1600 nm. The data are compared to the theoretical analyzer vectors of the design, which are plotted as continuous curves. Blue to red indicates the chromatic performance from 1000 nm to 1600 nm. In our analysis, the Mueller matrix of the linear polarizer is assumed to be that of an ideal linear polarizer based on specifications from Moxtek [31]. The Mueller matrix of the elliptical polarizer is the product of the linear polarizer Mueller matrix and the measured elliptical retarder Mueller matrix. In the measurement of the retarder Mueller matrix, the data point at 1100 nm is excluded because of inconsistent calibration result of the polarimeter at this wavelength (data not included) rather than the performance of the fabricated elliptical polarizers. We found that the high noise in the measurement at 1100 nm was caused by non-ideal polarization optics in the polarization state generator and the polarization state analyzer of the polarimeter, which were not manufactured perfectly, or optimized well, for 1100nm measurements. As expected, the analyzer vectors of the four elliptical polarizers forms a tetrahedron on the Poincaré sphere. This configuration, when used in a polarimeter, ensures an optimal reconstruction of the Stokes parameters [30]. The deviation of the analyzer vector $\tilde{a}$ characterizes the achromaticity of the optical filter and is

defined as:

$$\tilde{a} = \|a_\lambda - \bar{a}\|_2 \quad (4)$$

Here a_λ is the normalized analyzer vector at wavelength λ, $\bar{a}$ is the mean normalized analyzer vector across all wavelengths, and $\|\cdot\|_2$ represents the L^2-norm. Figure 5(b) compares the analyzer vector deviation parameter, $\tilde{a}$, between the theoretical design values and the measured results of the fabricated elliptical polarizers in the SWIR wavelength range. The original design had a constraint of less than 5% analyzer vector deviation in the wavelength region of 1000 nm to 1600 nm, as shown by the light green curve. For comparison, the analyzer vector deviation of the actual devices is plotted for each of the four test squares as well, denoted with the small circle marks. The overall analyzer vector deviation is found to be below 7% for all test squares and wavelengths, indicating good performance. It should be noted that the larger deviation from design at 1200 nm is due to small fabrication errors in thickness and deviations of the resonant wavelength, defined in Eq. (1), between the actual device and test samples.

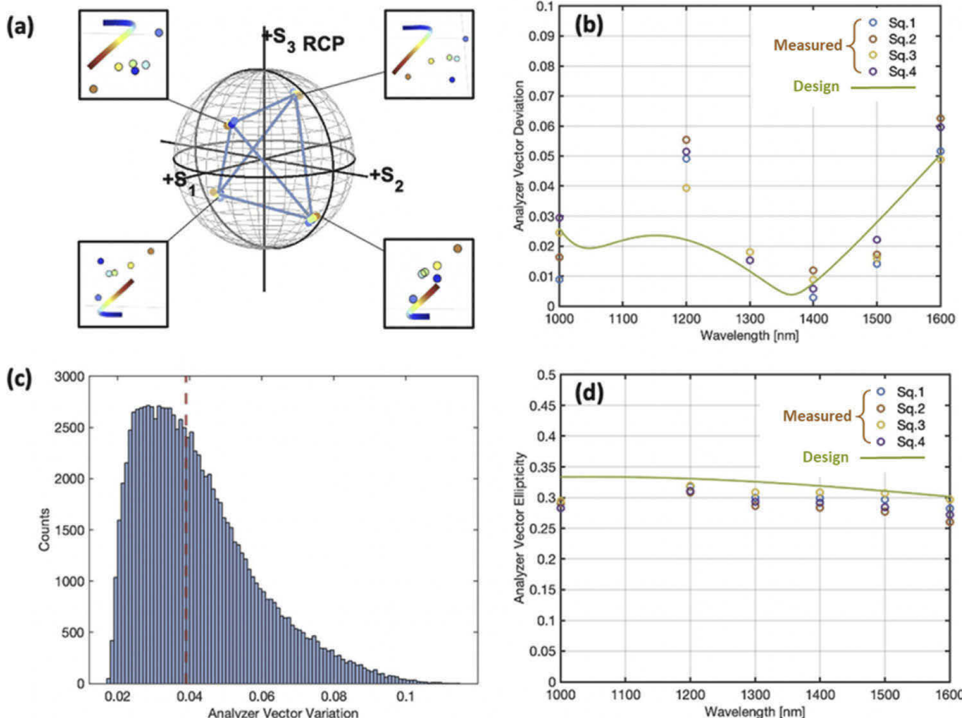

Fig. 5. (a) Analyzer vectors as a function of wavelength for the four elliptical polarizers are plotted on the Poincaré sphere, forming a regular tetrahedron. Measured analyzer vectors are data points, while the continuous curve represents the theoretical curve from 1000 nm (blue) to 1600 nm (red). (b) Comparison of the analyzer vector deviation between the theoretical design values and measured results shows good performance of the fabricated elliptical polarizers with an overall analyzer vector deviation below 7% for all the test squares in the SWIR wavelength range. (c) Results of the Monte Carlo simulation show how the analyzer vector deviates from the design when perturbed. The dashed curve indicates the median of the distribution. (d) Comparison of the ellipticity of the analyzer vectors between the theoretical design values and the measured results shows good uniformity and achromatic performance of the fabricated elliptical polarizers in the SWIR wavelength range.

Optics EXPRESS

The effect of fabrication errors, such as angle and thickness variations, on the analyzer vector is studied theoretically by carrying out a tolerance calculation in the form of a Monte Carlo simulation. The Monte Carlo simulation perturbs the design by changing the individual layer thickness by up to ±5% and the alignment angle of each of the individual layers by ±1°. The simulation was performed 100,000 times, and the analyzer vectors produced were compared to the original design's analyzer vector by computing the Euclidean distance between the two vectors. The results of the Monte Carlo simulation are presented in Fig. 5(c). The histogram shows a skewed distribution with the analyzer vector deviation below 0.05 for most of the simulations. The median of the distribution is about 0.04. The Euclidean distance between two vectors of this nature has a maximum value of two, representing analyzer vectors, which are orthogonal. Based on this analysis, we estimate the fabrication of the SWIR retarder has a variation in retarder thickness of less than ±5% and degree alignment accuracy of ±1 degree.

Another measure of the uniformity of the analyzer vectors as a function of wavelength is the ellipticity of the polarizer [14], which is defined as

$$\varepsilon_a = \frac{|a_3|}{\sqrt{a_1^2 + a_2^2 + a_3^2} + \sqrt{a_1^2 + a_2^2}} \tag{5}$$

Here $a_{1,}$ $a_{2,}$ $a_{3,}$ are the normalized components of the analyzer vector, i.e. the first row of the elliptical polarizers Mueller matrix. Figure 5(d) compares the ellipticity of the analyzer vectors between the theoretical design values and the measured results of the fabricated elliptical polarizers in the SWIR wavelength range. The measured results show good uniformity among the four test squares. The flatness of the curves through the SWIR wavelength range demonstrates excellent achromatic performance, in close agreement with the theoretical design.

5. Conclusions

We have shown experimentally that the single band dispersion model theory can be applied for characterizing retardance of LCP films within the wavelength range of 400 nm to 1600 nm. Based on this theory, we designed an SWIR achromatic elliptical polarizer consisting of a patterned linear polarizer and a patterned optical retarder. The linear polarizer is a patterned wire grid polarizer. The elliptical retarder was fabricated as a stack of three layers of nematic phase A-plate LCP films with retardance thicknesses of 0.7131, 1.4996, and 0.3937, respectively. For each LCP layer, four arrays of hexagonal patterns were realized with individual fast-axis orientations. For thinner LCP layers, e.g. 0.7131 and 0.3937 in retardance thicknesses, the LCP fast-axis orientations were realized by aligning with the LPP base layer in the direction defined by LPUV. To obtain alignment in thicker LCP films, e.g. 1.4996 in retardance thickness, an approach of two coatings of LCP was developed, where the first coating of LCP aligned with the LPP, and subsequently the second coating of LCP aligned in the same direction on the first LCP coating. Our results show that for an LCP layer of 1.4996 retardance thickness, the fast-axis angles can be aligned accurately within an array of hexagons with a center-to-center pitch of 900 µm. This LCP alignment approach extends the capabilities in fabrication where LCP alignment is needed; it also supports retarder designs for longer wavelengths requiring thicker aligned LCP films.

We measured the Mueller matrix of the four retarder arrays in the wavelength range of 1000 nm to 1600 nm. Our results show good uniformity and match the design parameters in both retardance and orientation angle. Analysis of the measured analyzer vector gives a deviation below 7% over the SWIR wavelength range, indicating a variation in retarder thickness of less than ±5% and an accuracy in LPUV angle within ±1 degree in the device fabrication. In addition, evaluation of analyzer vector ellipticity shows excellent achromatic performance in close agreement with the design. The patterned achromatic elliptical polarizer can be used for measurement of full Stokes parameters of broadband SWIR light.

Funding. Air Force Research Laboratory (FA8651-14-C-0108, FA8651-18-C-0066); National Science Foundation (2053754).

Acknowledgments. The authors thank Dr. Lu Lu and Dr. Junren Wang with Reality Labs at Meta for help and Mr. Ric Wehling and Dr. Nick Rummelt at AFRL for their continued support of this research.

Disclosures. The authors declare no conflicts of interest.

Data availability. Data underlying the results presented in this paper are not publicly available at this time but may be obtained from the authors upon reasonable request.

References

1. P. Hariharan and P. E. Ciddor, "Broad-band superachromatic retarders and circular polarizers for the UV, visible and near infrared," J. Mod. Opt. **51**(15), 2315–2322 (2004).
2. S. Pancharatnam, "Achromatic combination of birefringent plates," Proc. Indian Acad. Sci. **41**(4), 137–144 (1955).
3. J. Ma, J. S. Wang, C. Denker, and H. M. Wang, "Optical design of multilayer achromatic waveplate by simulated annealing algorithm," Chin. J. Astron. Astrophys. **8**(3), 349–361 (2008).
4. J. M. Herrera-Fernandez, J. L. Vilas, L. M. Sanchez-Brea, and E. Bernabeu, "Design of superachromatic quarterwave retarders in a broad spectral range," Appl. Opt. **54**(33), 9758–9762 (2015).
5. S. Shen, J. She, and T. Tao, "Optimal design of achromatic true zero-order waveplates using twisted nematic liquid crystal," J. Opt. Soc. Am. A **22**(5), 961–965 (2005).
6. K. Saha, A. K. Bhattacharya, and Chakraborty, "New achromatic quarter-wave combination of birefringent plates," Opt. Eng. **51**(1), 013001 (2012).
7. K. Saha, A. K. Bhattacharya, and Chakraborty, "Achromatic quarter-wave plate using crystalline quartz," Appl. Opt. **51**(12), 1976–1980 (2012).
8. X. Zhao, X. Pan, X. Fan, P. Xu, A. Bermak, and V. G. Chigrinov, "Patterned dual-layer achromatic micro-quarter-wave-retarder array for active polarization imaging," Opt. Express **22**(7), 8024 (2014).
9. X. Tu, L. Jiang, M. Ibn-Elhaj, and S. Pau, "Design, fabrication and testing of achromatic elliptical polarizer," Opt. Express **25**(9), 10355–10367 (2017).
10. G. Myhre, A. Sayyad, and S. Pau, "Patterned color liquid crystal polymer polarizers," Opt. Express **18**(26), 27777–27786 (2010).
11. J.-W. Moon, W.-S. Kang, H. yong Han, S. M. Kim, S. H. Lee, Y. gyu Jang, C. H. Lee, and G.-D. Lee, "Wideband and wide-view circular polarizer for a transflective vertical alignment liquid crystal display," Appl. Opt. **49**(20), 3875–3882 (2010).
12. J. E. Millerd and N. J. Brock, "Methods and apparatus for splitting, imaging, and measuring wavefronts in interferometry," U.S. Patent US6304330B1 (16 October 2001).
13. S.-W. Oh and T.-H. Yoon, "Achromatic wide-view circular polarizers for a high-transmittance vertically-aligned liquid crystal cell," Opt. Lett. **39**(16), 4683–4686 (2014).
14. R. A. Chipman, W. T. Lam, and G. Young, *Polarized Light and Optical Systems* (CRC, 2019).
15. V.L. Gamiz, "Performance of a four-channel polarimeter with low-light-level detection," in *Polarization: Measurement, Analysis, and Remote Sensing*, vol. 3121 D. H. Goldstein and R. A. Chipman, eds., International Society for Optics and Photonics (SPIE, 1997), pp. 35–46.
16. G. Myhre, W.-L. Hsu, A. Peinado, C. LaCasse, N. Brock, R. A. Chipman, and S. Pau, "Liquid crystal polymer full-stokes division of focal plane polarimeter," Opt. Express **20**(25), 27393–27409 (2012).
17. X. Tu, O. J. Spires, X. Tian, N. Brock, R. Liang, and S. Pau, "Division of amplitude RGB full-Stokes camera using micro-polarizer arrays," Opt. Express **25**(26), 33160–33175 (2017).
18. W.-L. Hsu, G. Myhre, K. Balakrishnan, N. Brock, M. Ibn-Elhaj, and S. Pau, "Full-Stokes imaging polarimeter using an array of elliptical polarizer," Opt. Express **22**(3), 3063–3074 (2014).
19. X. Zhao, A. Bermak, F. Boussaid, and V. G. Chigrinov, "Liquid-crystal micropolarimeter array for full Stokes polarization imaging in visible spectrum," Opt. Express **18**(17), 17776–17787 (2010).
20. K. L. Marshall, K. Adelsberger, G. Myhre, and D. W. Griffin, "The LCPDI: A Compact and Robust Phase-Shifting Point-Diffraction Interferometer Based on Dye-Doped LC Technology," Mol. Cryst. Liq. Cryst. **454**(1), 23/[425]–45/[447] (2006).
21. C.-T. Lee, H.-Y. Lin, and C.-H. Tsai, "Designs of broadband and wide-view patterned polarizers for stereoscopic 3D displays," Opt. Express **18**(26), 27079–27094 (2010).
22. C.-T. Lee and H. Y. Lin, "Ultra-wide-view patterned polarizer type stereoscopic LCDs using patterned alignment," Opt. Express **20**(2), 1700–1705 (2012).
23. S.-W. Oh, S.-H. Kim, J.-M. Baek, and T.-H. Yoon, "Design of an achromatic wide-view circular polarizer using normal dispersion films," J. Inf. Disp. **20**(1), 25–30 (2019).
24. M. P. Wen, C. Mahajan, and Rosenblatt, "Ultrahigh-resolution liquid crystal display with gray scale," Appl. Phys. Lett. **76**(10), 1240–1242 (2000).
25. T. Ishinabe, T. Miyashita, and T. Uchida, "47.2: Novel Wide Viewing Angle Polarizer with High Achromaticity," SID Symp," SID Symposium Digest of Technical Papers **31**(1), 1094–1097 (2000).
26. M. B. Ko and K. H. Park, "Polarizing plate for oled and optical display including the same," U.S. Patent US9563000B2 (7 February 2017).

27. P. Li, G. Kang, I. Vartiainen, F. Wang, Y. Liu, and X. Tan, "Investigation of achromatic micro polarizer array for polarization imaging in visible-infrared band," Optik **158**, 1427–1435 (2018).
28. C. Hardy, C. H. Lee, and F. M Reininger, "Calibration, registration, and super resolution with bio-inspired cameras," *Proceedings of the 2017 International Conference on Computer Graphics and Digital Image Processing*, ACM, Article No.: 16, Pages 1-7 (July 2017).
29. S. T. Wu, "Birefringence dispersions of liquid crystals," Phys. Rev. A **33**(2), 1270–1274 (1986).
30. D. S. Sabatke, M. R. Descour, E. L. Dereniak, W. C. Sweatt, S. A. Kemme, and G. S. Phipps, "Optimization of retardance for a complete Stokes polarimeter," Opt. Lett. **25**(11), 802–804 (2000).
31. M. C. George, J. Bergquist, B. Wang, R. Petrova, H. Li, and E. Gardner, "An improved wire grid polarizer for thermal infrared applications," Proc. Of SPIE **8613**, 86131I (2013).
32. S. Kumar, J. H. Kim, and Y. Shi, "What aligns liquid crystals on solid substrates? The role of surface roughness anisotropy," Phys. Rev. Lett. **94**(7), 077803 (2005).
33. O. Yaroshchuk and Y. Reznikov, "Photoalignment of liquid crystals: basics and current trends," J. Mater. Chem. **22**(2), 286–300 (2012).

67.1.208.84 {ts '2022-03-04 16:36:16'}